

An Inter-shaft Bearing Fault Diagnosis Dataset from an Aero-engine System

Lei Hou^{1*}, Haiming Yi¹, Yuhong Jin¹, Min Gui², Lianzheng Sui², Jianwei Zhang², Yushu Chen¹

1) *School of Astronautics, Harbin Institute of Technology, Harbin 150001, China;*

2) *Factory of Xiang Yang Hang Tai Power Machinery, Xiangyang 441000, China*

ABSTRACT

In this paper, the aero-engine test with inter-shaft bearing fault is carried out, and a dataset is proposed for the first time based on the vibration signal of rotors and casings. First, a test rig based on a real aero-engine is established, driven by motors and equipped with a lubricating system. Then, the aero-engine is disassembled and assembled following the specification process, and the inter-shaft bearing with artificial fault is replaced. Next, the aero-engine test is conducted at 28 groups of high and low pressure speeds. Six measuring points are arranged, including two displacement sensors to test the displacement vibration signals of the low pressure rotor and four acceleration sensors to test the acceleration vibration signals of the casing. The test results are integrated into an inter-shaft bearing fault dataset. Finally, based on the dataset in this paper, frequency spectrum, envelope spectrum, CNN, LSTM and TST are used for fault diagnosis, and the results are compared with those of CWRU and XJTU datasets. The results show that the characteristic fault frequency cannot be found directly in the spectrum and envelope spectrum corresponding to this paper's dataset but in CWRU and XJTU datasets. Using CNN, LSTM and TST for fault diagnosis of the dataset in this paper, the accuracy is 83.13%, 85.41% and 71.07%, respectively, much lower than the diagnosis results of CWRU and XJTU datasets. It can be seen that the dataset in this paper is closer to the actual fault diagnosis situation and is a more challenging dataset. This dataset provides a new benchmark for the validation of fault diagnosis methods. Mendeley data: <https://github.com/HouLeiHIT/HIT-dataset>.

Keywords: inter-shaft bearing, fault diagnosis, aero-engine test, dataset.

1. Introduction

Aero-engine is the core component of an aircraft, and its stable operation guarantees the safe flight of the aircraft. In a dual-rotor aero-engine, the aircraft rolling bearing is a crucial load-bearing component, and the operating environment is harsh and highly prone to failure, causing severe accidents. Therefore, establishing aircraft rolling bearing fault datasets and conducting research on aero-engine fault diagnosis can help to timely identify the early minor fault characteristics of aircraft rolling bearings and avoid accidents^[1-3].

In existing research, the fault diagnosis of aircraft rolling bearings is mainly conducted through bearing vibration signals. Hou et al^[4] proposed a feature extraction

technique for inter-shaft bearing faults under noisy conditions, using Laplace wavelet and orthogonal matching pursuit algorithm combined with sparse representation theory. The method effectively extracted weak-bearing fault features by identifying the transient shock component. Yang et al^[5] focused on high-speed rotor systems and established a symmetrical rigid bearing-rotor model. They took the envelope analysis to research the dynamic response and qualitatively verified the response by the experimental results. Wang et al^[6] proposed an inter-shaft bearing fault diagnosis method called Improved Spiking Neural Network (ISNN), the ISNN was superior to previous Spiking Neural Network (SNN). Yu et al^[7] proposed an algorithm that combines information fusion, wavelet transform (WT), singular value decomposition (SVD), Katz fractal dimension, and Cross-Correlation Function (CCF), called CCF-WT-SVD-Katz. Each part of the algorithm could achieve signal denoising, enhance reconstruction and extract fault features. Liu et al^[8] developed a combined model of LSTM network with deep CNN and conducted theoretical and experimental research. The results showed that the prediction accuracy of the method reached 99.94% and 98.67%, which was better than the single deep CNN and LSTM. Liu et al^[9] proposed a combined method of deep learning and particle filter. The validity of the method was verified by whole lifetime test of bearings, and the results showed that this method got a prediction accuracy of 2.19%, 0.93%, and 1.43% higher than RMS values. Zhang et al^[10] developed a blind extraction method for multi-channel fault signals based on the CCA criterion, which took the bearing fault frequency to calculate the delay parameter. The simulation and experimental results demonstrated that this method had better accuracy and convergence speed. Hou et al^[11] developed a Siamese Multiscale Residual Feature Fusion Network (SMSRFFN) for small-sample conditions of aero-engine bearing fault diagnosis. Conducting tests by existing datasets and the results demonstrated the validity of the SMSRFFN in fault diagnosis accuracy under minor sample conditions. Pan et al^[12] proposed a combined of Intrinsic Time-scale Decomposition (ITD) and Singular Value Decomposition (SVD) to diagnose compound bearing faults. Compared with ITD and PCA methods, the results showed that the ITD-SVD method gets a higher accuracy under noise. Wang et al^[13] developed a planetary gearbox fault diagnosis method by conducting a transferable deep Q network (TDQN). The test results showed that the TDQN got an accuracy of 98.53% in a source task, 99.63% and 98.37% in two target tasks.

Datasets are crucial in verifying the effectiveness of fault diagnosis methods, and the common fault diagnosis datasets include Case Western Reserve University (CWRU) dataset^[14] and Xi'an Jiaotong University (XJTU) dataset^[15], etc. These datasets provide data support for the validation of bearing fault diagnosis methods. However, these datasets have a single research object and are mainly focused on bearing vibration signals, which cannot meet the fault diagnosis needs of other machines. Therefore, some researchers established new datasets based on different machines. Kumar et al^[16] took vibration analysis for motor bearing fault detection using triaxial vibration data acquired with a MEMS-based accelerometer and NI myRIO, and established a motor bearing fault dataset. The dataset included healthy and faulty bearing conditions under different loads and was useful for assessing new fault diagnosis methods. Jung et al^[17]

established a time-series dataset based on rotating machines' temperature, vibration, driving current and acoustic data. The rotating machine conditions included normal, shaft misalignment, bearing faults, and rotor unbalance. The dataset could be used to verify methods for rotating machines' fault diagnosis. Lessmeier et al^[18] presented a benchmark dataset of rolling bearings with damage, which used the motor current signal of an electromechanical drive system as data. The dataset included damage in external bearings with a wide distribution of bearing damage. The classification accuracy was lower compared to classifications based on vibration signals, which meant it could be used for further research. In addition, the image-based bearing fault diagnosis^[19], helpful motor life estimation^[20-22], bearing life prediction^[15,23-26] and gear fault diagnosis^[27] also had corresponding datasets for research. It can be seen that the corresponding dataset is crucial in the field of fault diagnosis, health monitoring, and anomaly detection of rotating machinery.

To sum up, in the existing research on machine learning methods for aircraft rolling bearing fault diagnosis of an aero-engine, the training and testing set is based on the publicly released datasets of the bearing fault. Replacing inter-shaft bearings is complicated and difficult, so there are no publicly released datasets about the aircraft rolling bearing fault data based on the aero-engine signals of the rotors and casings. In this paper, we build a test rig, take the aero-engine tests with inter-shaft bearing faults, and establish a dataset based on the result of the tests. The main contributions of this paper are listed as follows.

- (1) An inter-shaft bearing fault dataset is released for the first time based on the aero-engine system, which comes from the vibration response of the aero-engine rotor and casings rather than just from bearing test bench data. The released dataset is closer to the aero-engines actual excitation state and vibration coupling.
- (2) The dataset includes three types of data: healthy, inner ring fault, and outer ring fault. The rotor speed range ranges from 1000r/min to 6000r/min. The measurement points are arranged on the rotor and casings, and the vibration signals include displacement and acceleration signals.
- (3) The paper applies frequency spectrum, envelope spectrum, CNN, LSTM, and TST methods for preliminary dataset analysis and finds that the dataset can be diagnosed using existing fault diagnosis methods, which indicates universality. Comparing the diagnosis results with those of the XJTU and CWRU datasets, it is found that the fault diagnosis of the dataset in this paper is more complicated, which provides a challenging new benchmark for performance evaluation of subsequent fault diagnosis methods.

The rest of this paper is arranged as follows. In Section II, the structure of the test rig is described. In Section III, the procedure of the test was introduced. Section IV establishes the dataset and does inter-shaft bearing fault diagnosis analysis based on it. Section V summarizes the conclusions of this paper.

2. Aeroengine Tests

2.1 Test Rig of Aero-engine

Vibration analysis of aero-engines plays a critical role in ensuring their safety and reliability during operation. To accurately obtain the vibration response of an aero-engine and simulate the inter-shaft bearing faults, a test rig that replicates the real-life operating conditions is essential. In this study, we established a test rig based on a real aero-engine to measure the vibration response of the engine during operation. The test rig comprises three main components: a modified aero-engine, a motor drive system, and a lubricant system. The modified aero-engine serves as the core component of the test rig and is responsible for generating the vibration signals during operation. The motor drive system, on the other hand, provides the necessary driving force to run the aero-engine at different speeds and loads, while the lubricant system ensures that the engine runs smoothly and efficiently. The physical map of the test rig is shown in Fig. 1.

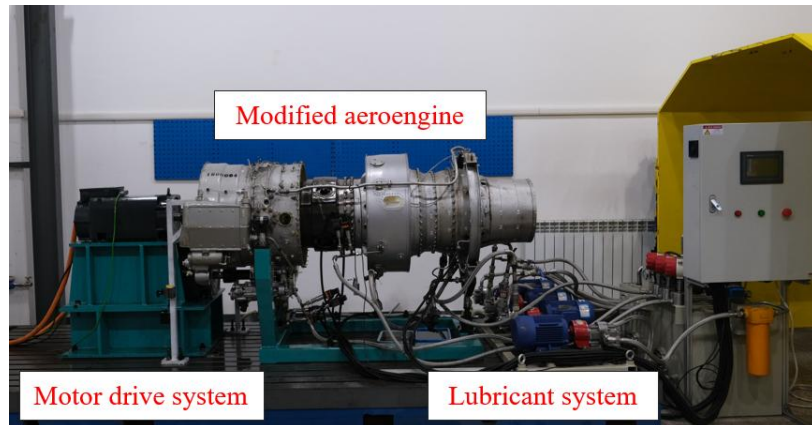


Fig. 1 The test rig based on a real aero-engine.

The modified aero-engine utilized in the test rig involves the removal of the rotor blades, combustion chamber, and certain accessory casings. And the crucial dual-rotor structure, which constitutes the main component of the aero-engine, is preserved. This dual-rotor structure includes both the low pressure (LP) compressor and high pressure (HP) compressor and the LP turbine and HP turbine. The main load-bearing casing, inter-shaft bearing, and five support bearings are also preserved. The dual-rotor structure is depicted in Fig. 2, while the inter-shaft bearing is displayed in Fig. 3. Tab. 1 provides the pertinent parameter information.

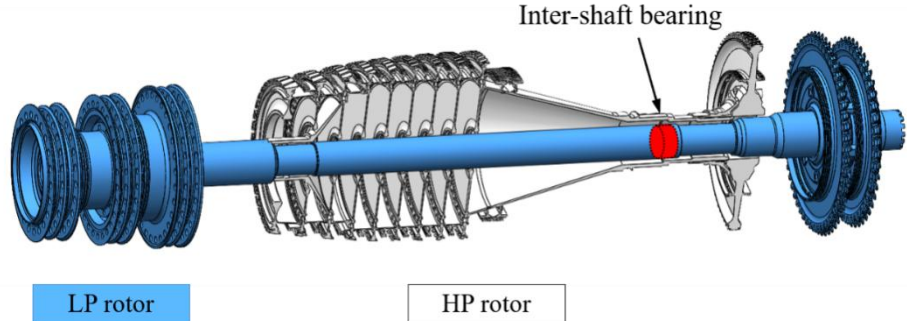


Fig. 2 Three-dimensional model of dual-rotor structure.

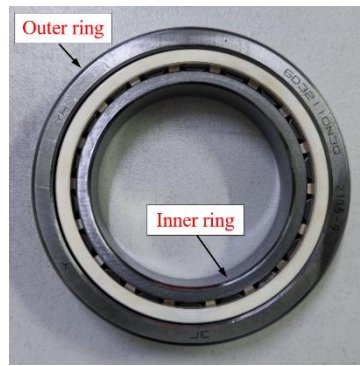


Fig. 3 The inter-shaft bearing.

Tab. 1 Parameter information of inter-shaft bearing.

| Parameter | Value |
|----------------------------|-------|
| Number of rolling elements | 15pc. |
| Diameter of inner ring | 30mm |
| Diameter of outer ring | 65mm |
| Diameter of pitch circle | 55mm |
| Rolling element diameter | 7.5mm |
| Nominal pressure angle | 0°N |

In the motor drive system, two motors are utilized in the test rig to drive the LP rotor and HP rotor. The LP motor directly drives the LP rotor, while the HP motor drives the HP rotor through a speed-raising gearbox. Fig. 4 depicts the motors employed in the test rig, and Tab. 2 presents the parameter information of the motors, including the rated current, rated moment and rated speed. The motors play a crucial role in the test rig, as they drive the rotors and generate the vibration responses. Therefore, selecting suitable motors with appropriate parameters is essential to guarantee the accuracy and reliability of the test results. Based on the requirements of the test rig, the LP motor and HP motor were chosen carefully, ensuring that they meet the necessary specifications for the test rig.

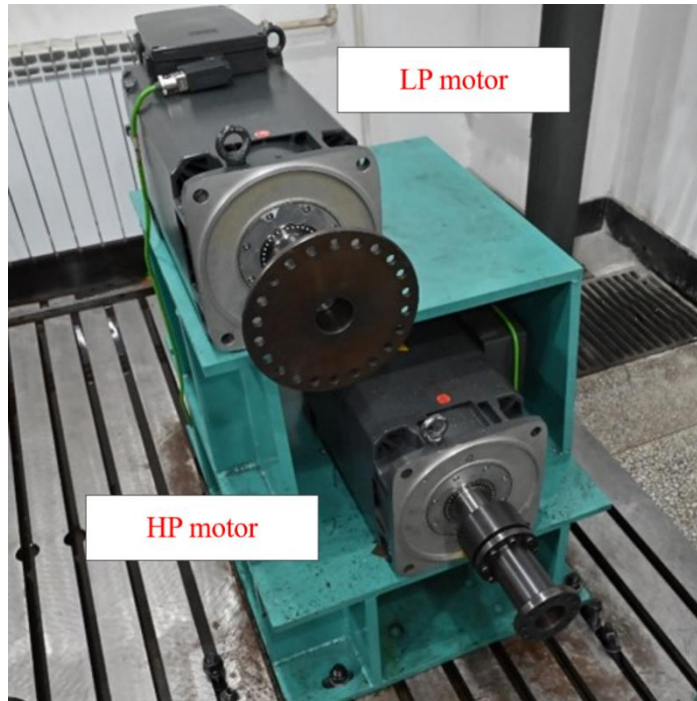


Fig. 4 The LP motor and HP motor.

Tab. 2 Information of LP and HP motors.

| Name | Manufacturer | Model number | Parameter | Value |
|----------|--------------|---------------|-----------|----------|
| LP motor | SIEMENS | 1PH8137-1SG03 | I_{max} | 152A |
| | | | M_{max} | 340Nm |
| | | | n_{max} | 10000rpm |
| HP motor | SIEMENS | 1PH8137-1SS03 | I_{max} | 130A |
| | | | M_{max} | 320Nm |
| | | | n_{max} | 15000rpm |

A lubricant system is equipped on the test rig for lubricating and cooling effects. It includes three oil-feed pumps, an oil scavenger pump, and a heat pump prepared with temperature sensors, which enable the system to realize the function of temperature control and maintain a stable temperature for optimal performance. The oil-feed pumps are shown in Fig. 5.



Fig. 5 The oil-feed pumps.

In addition, to ensure the safety of testers and equipment, three metal protective covers are installed to prevent any accidents caused by falling parts. The monitoring system is also set up to detect any potential anomalies in real-time, enabling prompt actions. The protective metal covers and monitoring system can be observed in detail in Fig. 6, providing a comprehensive overview of the safety measures in place for the test rig.

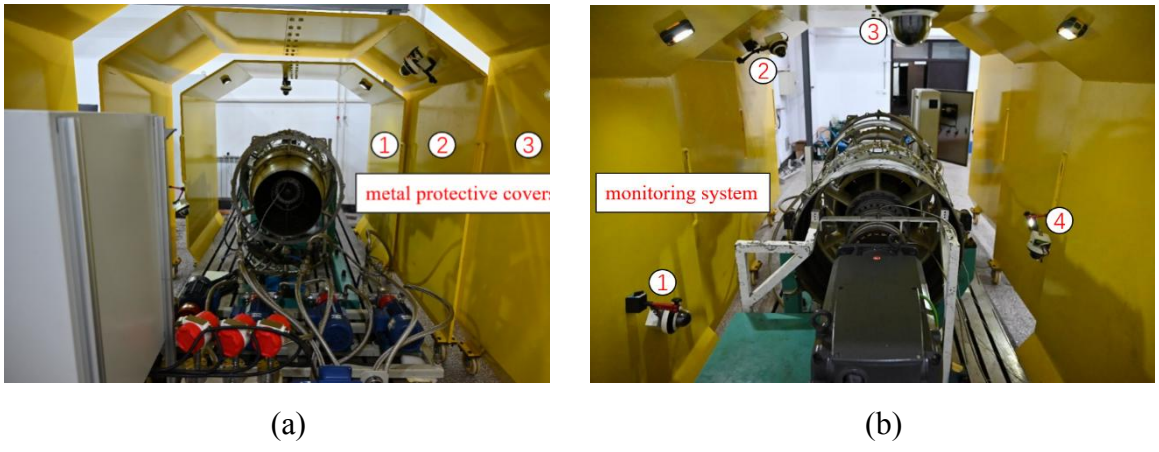


Fig. 6 (a) Metal protective covers. (b) Monitoring system.

2.2 Artificial Faults of Inter-shaft Bearing

The study of bearing fault diagnosis often involves creating artificial faults and conducting simulation tests to obtain fault characteristics. This approach can also be applied to the inter-shaft bearing fault diagnosis of aero-engines. Artificial faults, such as those found in the inner and outer rings, can cause periodic shocks on the rolling balls during rotation. These periodic shock signals are similar to those caused by actual faults, making them an effective tool for diagnosing faults.

This study sequentially fitted three inter-shaft bearings with artificial faults into the modified aero-engine. These included one bearing with an outer ring fault and two with inner ring faults. The artificial faults were created by wire cutting, as shown in Fig. 7, and the relevant bearing information and fault dimensions are listed in Tab. 3.



(a)

(b)

(c)

Fig. 7 The inter-shaft bearings with artificial (a) outer ring fault. (b) inner ring fault. (c) inner ring fault.

Tab. 3 Fault information of inter-shaft bearings with artificial fault.

| No. | Fault Position | Depth of fault/mm | Length of fault/mm |
|-----|----------------|-------------------|--------------------|
| 1 | Outer ring | 0.5 | 0.5 |
| 2 | Inner ring | 0.5 | 0.5 |
| 3 | Inner ring | 0.5 | 1.0 |

3. Preparation of Test

To obtain the vibration characteristic of the aero-engine under fault conditions, the inter-shaft bearing needs to be replaced by those with artificial faults in sec 2.2. The complex structure of an aero-engine makes it difficult to disassemble and assemble, therefore, there is almost no research involved in the replacement of inter-shaft bearings of an aero-engine in the existing research. In this paper, testers disassemble the aero-engine, replace the inter-shaft bearing, assemble the aero-engine, and install the aero-engine on the test rig under the guidance of professional engineers. A custom-made assembly wagon holds the aero-engine in place during the disassembly and assembly process. After replacing the inter-shaft bearing and assembling the aero-engine, the aero-engine can be installed on the test rig and connected to the motor drive and lubricant systems. The specific steps of the disassembly and assembly process are shown as follows.

3.1 Preparatory Work

It is necessary to ensure the power and oil are off before the disassembly begins. And then, the aero-engine needs to be separated from the motor drive and lubricant systems. The aero-engine is connected to the motors by couplings and wire and with a lubricant system by oil pipes. After secession, the crane is used to lift the aero-engine and install it on the custom-made assembly wagon. The process of preparatory work is shown in Fig. 8.

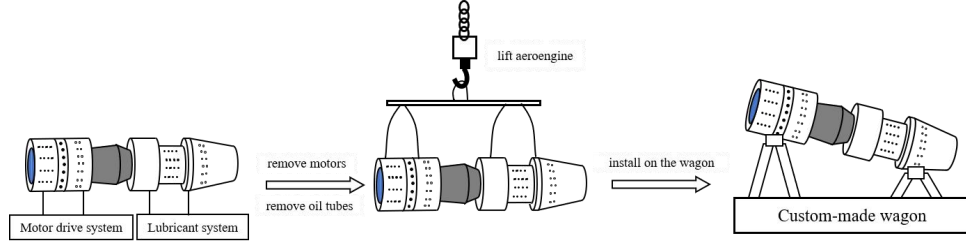


Fig. 8 The schematic diagram of preparatory work.

3.2 Disassemble Aeroengine

It's a complex process to disassemble the aero-engine, and many customized tools and wagons are used in the disassembly process. The disassembly process can be roughly divided into four steps.

Step 1, the support and transmission components are disassembled in sequence, including the fan casing, transfer gearbox, main transmission casing, central driving shaft, and tail casing, as shown in Fig. 9.

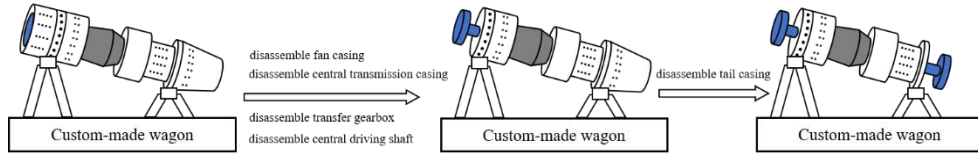


Fig. 9 The schematic diagram of step 1.

Step 2, the components related to the LP turbine disassembled, such as LP compressor disks, LP turbine disks, LP turbine shaft, and LP turbine blades, as shown in Fig. 10.

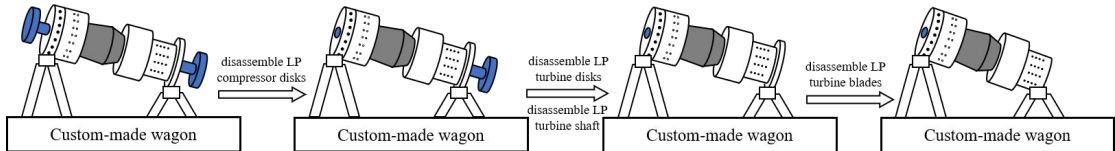


Fig. 10 The schematic diagram of step 2.

Step 3, the high-pressure (HP) turbine components are disassembled, such as HP turbine disk, HP turbine shafts, and HP turbine blade, as shown in Fig. 11.

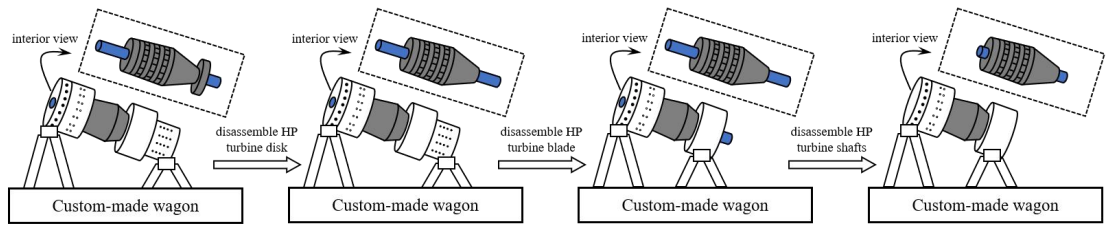


Fig. 11 The schematic diagram of step 3.

Step 4, the HP casing and the combustor casing are disassembled, and then the crane can lift the HP rotor. The inter-shaft bearing remains in a tubular structure called a combustion cylinder. To remove it, the tubular structure needs to be heated to 205°C, and customized tools can detach the inter-shaft bearing. The primary process is shown in Fig. 12.

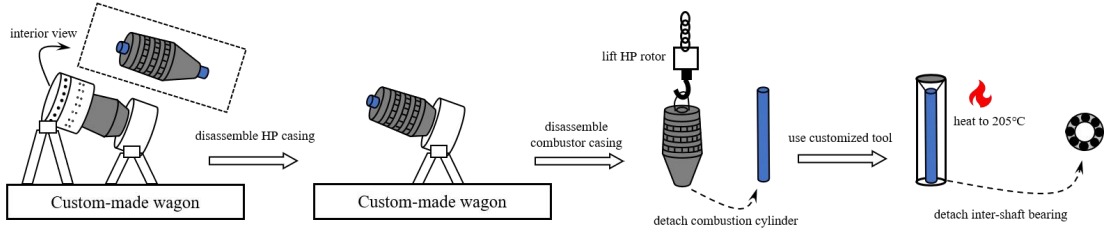


Fig. 12 The schematic diagram of step 4.

3.3 Assemble Aeroengine

The assembly process is the reverse process of disassembly. After replacing the inter-shaft bearing to be tested, the components are assembled following steps 4 through 1 in sec. 2.3.2. After assembling the aero-engine and installing it on the test rig, the motor drive system and the lubricant system need to be connected to the aero-engine, then the test rig is ready for the test.

3.4 Test of Aeroengine with Inter-shaft Bearing Fault

The arrangement of testing points is shown as Fig. 13. Two eddy current sensors are used to measure the horizontal and vertical vibration displacement response of the LP rotor. Four acceleration sensors are used to measure the normal vibration acceleration response of the casings, the information of the sensors is shown in Tab. 4. The number of testing points corresponds to the channel number in the dataset.

Tab. 4 Information of sensors

| Sensor type | Sensor model | Measure point |
|--------------|-------------------|---------------|
| Displacement | KISTLER 8776A50M1 | 1, 2 |
| Acceleration | K9000XL | 3, 4, 5, 6 |

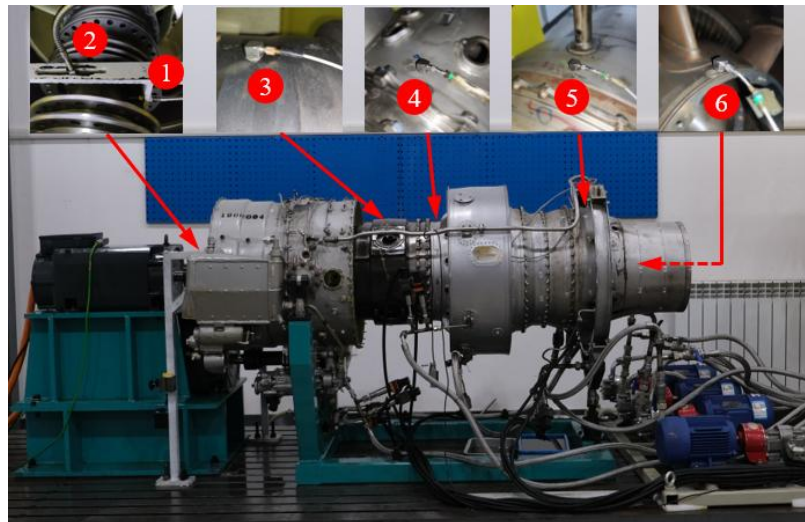


Fig. 13 The arrangement of testing points.

After ensuring the regular operation of the test rig and the correct arrangement of measuring points, the test can proceed as planned. The displacement and acceleration sensors collect signals and input them through the TRION-2402-dACC differential multifunctional module. These signals are analyzed by the DEWETRON DEWE2-M7 and saved on the computer for later analysis. The sampling frequency is set to 25000 Hz. The testers control and monitor the test via computer, and the real-time test status is displayed on screens, as shown in Fig. 14. The test plan for rotor speed is presented in Tab. 4. During the test, the signals recorded by the sensors are stored in the computer while both HP and LP rotors accelerate to the designated speed. For each bearing, a total of 28 data groups should be collected before the aero-engine is disassembled to replace the next bearing under test.

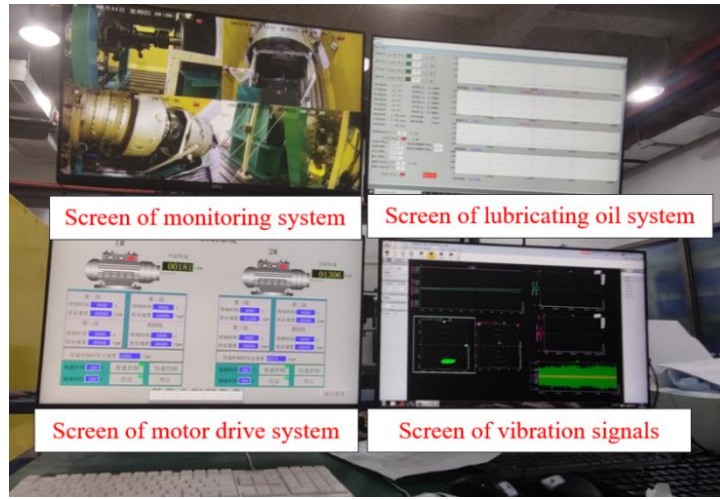


Fig. 14 The monitoring screen of the test.

Tab. 5 The test plan for rotor speed.

| LP speed (r/min) | HP speed (r/min) | Speed ratio | LP speed (r/min) | HP speed (r/min) | Speed ratio |
|---------------------|---------------------|-------------|---------------------|---------------------|-------------|
| 1000 | 1200 | 1.2 | 4400 | 5280 | 1.2 |
| 1500 | 1800 | 1.2 | 4500 | 5400 | 1.2 |
| 2000 | 2400 | 1.2 | 4600 | 5520 | 1.2 |
| 2500 | 3000 | 1.2 | 4700 | 5640 | 1.2 |
| 3000 | 3600 | 1.2 | 4800 | 5760 | 1.2 |
| 3500 | 4200 | 1.2 | 4900 | 5880 | 1.2 |
| 3600 | 4320 | 1.2 | 5000 | 6000 | 1.2 |
| 3700 | 4440 | 1.2 | 3000 | 3600 | 1.2 |
| 3800 | 4560 | 1.2 | 3000 | 3900 | 1.3 |
| 3900 | 4680 | 1.2 | 3000 | 4200 | 1.4 |
| 4000 | 4800 | 1.2 | 3000 | 4500 | 1.5 |
| 4100 | 4920 | 1.2 | 3000 | 4800 | 1.6 |
| 4200 | 5040 | 1.2 | 3000 | 5100 | 1.7 |
| 4300 | 5160 | 1.2 | 3000 | 5400 | 1.8 |

4. Datasets and Benchmark Study

4.1 Datasets of Aeroengine with Inter-shaft Bearing Fault

The test is carried out five times and five datasets of three states of inter-shaft bearings are obtained, which are stored in the form of a time series. Each dataset is stored as a three-dimensional array, such as $[A]_{a \times b \times c}$. Raw data is a long time series of 15 seconds of sampling. The sampling frequency is 25000Hz. The raw data is segmented and truncated for subsequent analysis into a short time series containing 20480 data points. After eliminating invalid data, 2412 sets of data are retained in the datasets in total.

For each dataset, each row corresponds to the same test, the first two columns store the displacement response, and columns 3 through 6 store the acceleration response. Column 7 stores the high and low speed information of this test. In the datasets, the states of inter-shaft bearings are distinguished by labels, that label ‘0’ represents ‘health inter-shaft bearing’, label ‘1’ means ‘inter-shaft bearing with inner ring fault’ and label ‘2’ represents ‘inter-shaft bearing with outer ring fault’. The label information is stored at column 8. The schematic diagram of the datasets is shown in Fig. 15 and the essential information of the datasets is shown in Tab. 5.

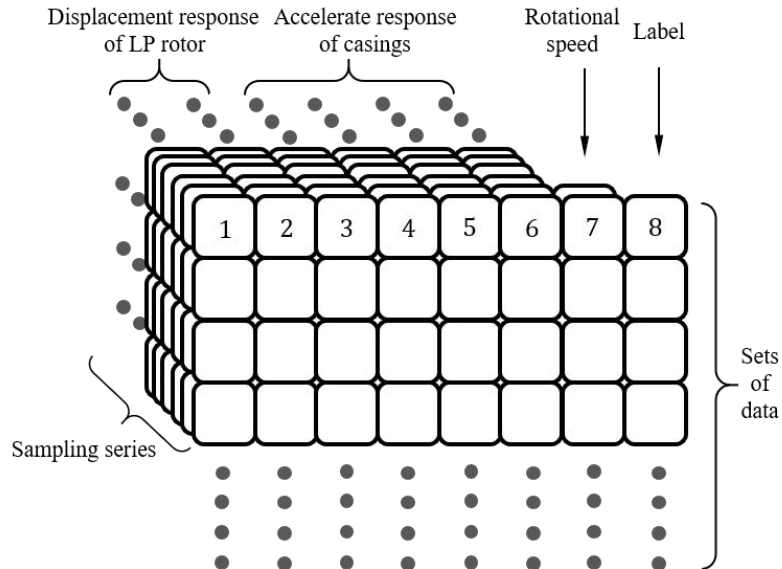


Fig. 15 The schematic diagram of the datasets.

Tab. 6 Information of the datasets.

| Name | Fault position | Depth of fault/mm | Length of fault/mm | Sampling frequency/Hz | LP and HP speed(r/min) | Length per series | Number of series |
|-------|----------------|-------------------|--------------------|-----------------------|------------------------|-------------------|------------------|
| data1 | none | 0 | 0 | 25000 | LP speed range: | 20480 | 504×6 |
| data2 | none | 0 | 0 | 25000 | 1000~5000 | 20480 | 450×6 |
| data3 | inner ring | 0.5 | 0.5 | 25000 | HP speed range: | 20480 | 504×6 |

| | | | | | | | |
|-------|------------|-----|-----|-------|-----------|-------|----------------|
| data4 | inner ring | 0.5 | 1.0 | 25000 | 1200~6000 | 20480 | 504×6 |
| data5 | outer ring | 0.5 | 0.5 | 25000 | | 20480 | 450×6 |

4.2 Benchmark Study of Spectrum Analysis

In the research of bearing fault diagnosis, frequency spectrum analysis is a common method. The characteristic frequency peaks on the frequency spectrum can be used to determine whether a fault occurs. As for the original vibration signals with excessive noise components, the envelope signal can be obtained by the envelope transformation of the original signal to reduce the interference of noise components. In order to compare the dataset in this paper with the CWRU and XJTU datasets, a group of signals with bearing inner ring fault is taken as an example, the information of these dataset signals is shown in Tab. 6. the acceleration time histories of three datasets are shown as Fig. 16, and the frequency spectrums are shown as Fig. 17.

Tab. 7 Information of the compared signals

| Datasets | Fault position | Fault type | Size of fault | Sampling frequency | Motor speed/rpm | Signal type |
|----------|----------------|----------------|---------------|--------------------|-----------------|--------------|
| Proposed | inner ring | Artificial | 0.5 | 25000Hz | 2000/2400 | Acceleration |
| CWRU | inner ring | Artificial | 0.5334 | 12000Hz | 1797 | Acceleration |
| XJTU | inner ring | Run-to-failure | None | 25600Hz | 2250 | Acceleration |

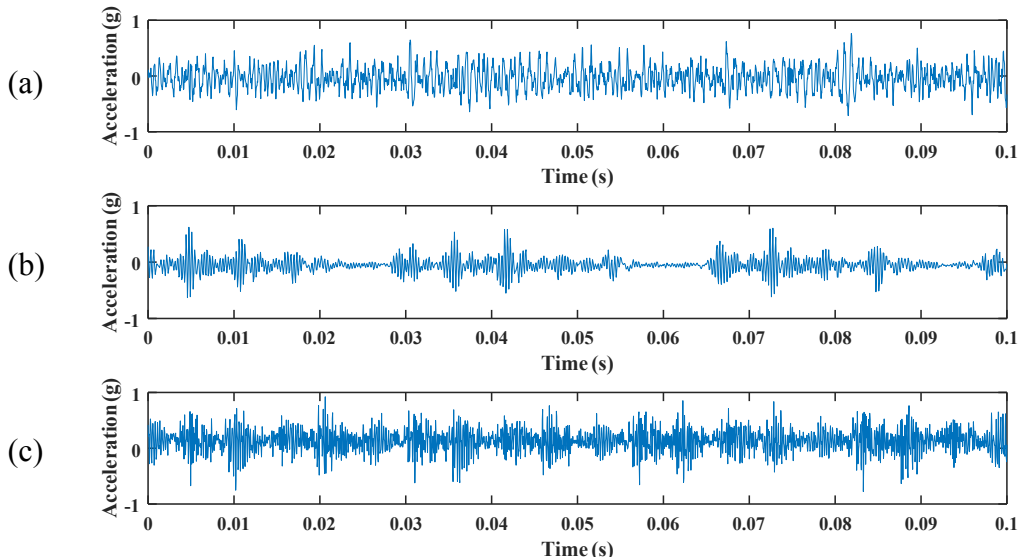


Fig. 16 The time histories of bearing with inner ring fault. (a) Dataset of this paper. (b) CWRU dataset. (c) XJTU dataset.

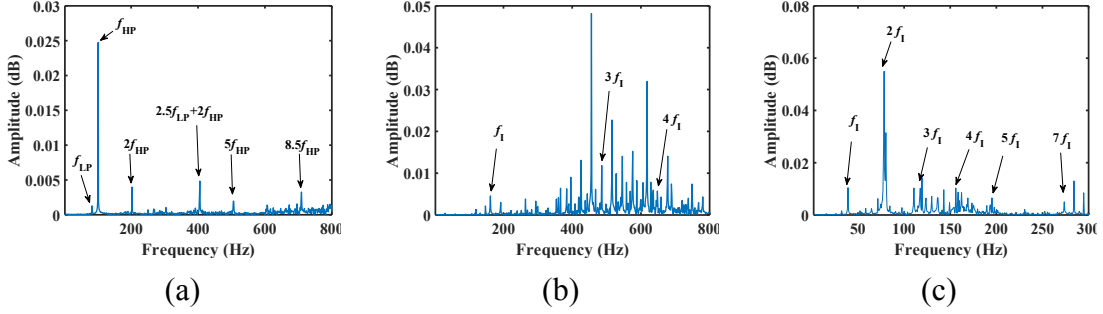


Fig. 17 The frequency spectrums of bearing with inner ring fault. (a) Dataset of this paper. (b) CWRU dataset. (c) XJTU dataset.

The acceleration time histories in Fig. 16 show that the vibration signal of this paper is closer to a random signal, while the signals of CWRU and XJTU exhibit a more pronounced impact phenomenon. From the frequency spectrums shown in Fig. 17, it can be seen that there are lots of frequency components that appear in the frequency spectrums. In the frequency spectrum of the dataset of this paper in Fig. 17(a), the main frequency components are the frequency f_{HP} and its doubling frequencies $2f_{HP}$, $5f_{HP}$ and so on. The combined frequency $2.5f_{LP}+2f_{HP}$ also corresponds to a frequency peak. But the inner fault characteristic frequency f_I can't be found in the frequency spectrum, so it's hard to fault diagnosis directly by frequency spectrum. While in the frequency spectrum of CWRU in Fig. 17(b), the inner ring fault characteristic frequency f_I and its doubling frequencies $3f_I$ and $4f_I$ can be found and in the frequency spectrum of XJTU in Fig. 17(c), the inner ring fault characteristic frequency f_I and its doubling frequencies $2f_I$, $3f_I$, $4f_I$, $5f_I$ and $7f_I$ can be found, these noticeable fault features can be directly used for fault diagnosis.

In summary, it is impossible to analyze the frequency spectrum of the dataset in this paper for the fault diagnosis. The main reason is that the testing point is arranged on the casing. Therefore, the fault characteristics appear distorted in the transmission process. During the transmission process, the signal of fault character is tapering off and the collisions between connected structures may produce noise, which makes the composition of the vibration signal more complex. In addition, there are also many other frequency components in the frequency spectrum of CWRU and XJTU datasets besides fault features. To reduce the interference of noise signal and amplify the impact effect, the envelope signals obtained by the envelope transformation are shown in Fig. 18 and the envelope spectrums are shown in Fig. 19.

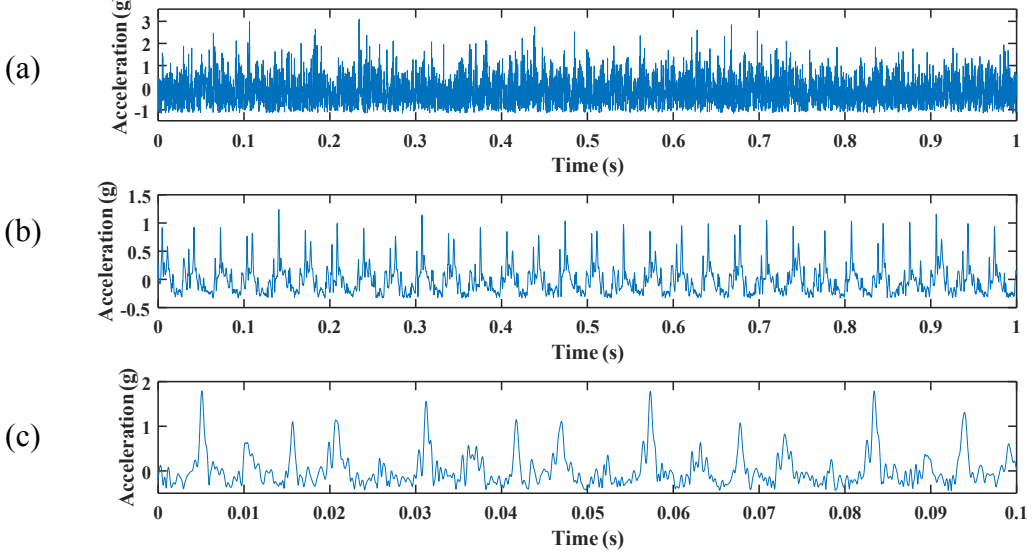


Fig. 18 The envelope signals of bearing with inner ring fault. (a) Dataset of this paper. (b) CWRU dataset.
(c) XJTU dataset.

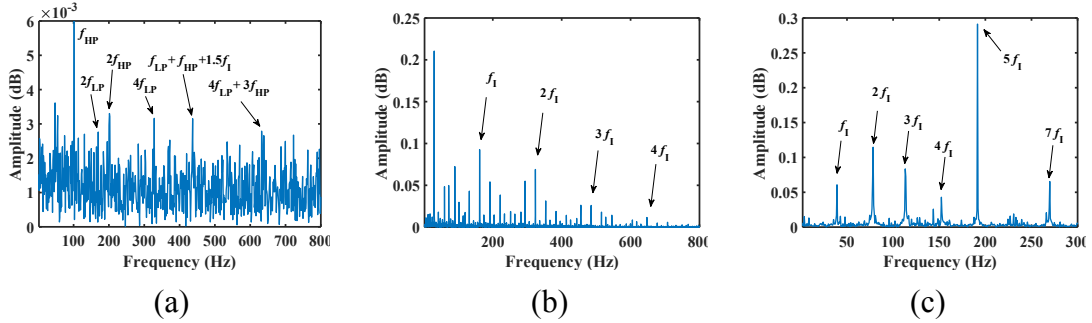


Fig. 19 The envelope spectrums of bearing with inner ring fault. (a) HIT dataset. (b) CWRU dataset. (c) XJTU dataset.

From the envelope signals in Fig. 18, it can be seen that the envelope signals in Fig. 18(a) don't show as significant periods, while the signals from the CWRU and XJTU datasets exhibit significant periodicity. In the envelope spectrums of CWRU and XJTU datasets in Fig. 19(b) and Fig. 19(c), the inner ring fault characteristic frequencies are more evident than in frequency spectrums. In the envelope spectrums of the dataset of this paper in Fig. 19(a), the frequency components are more complex, which means the fault characteristics are distorted seriously during the transmission. The envelope spectrums have more combined frequency components, especially those related to f_{LP} and f_{HP} . The fault frequencies appear in Fig. 19(a) as the form of combined frequencies $f_{LP}+f_{HP}+1.5f_I$, but the amplitude of peaks in the envelope spectrums are approximate and the peaks related to the fault frequencies are not the highest. That means the envelope spectrum is hard to be used as the basis for fault diagnosis. The fault characteristics can't be separated by traditional fault diagnosis methods such as spectrum and envelope analysis. This also indicates that the inter-shaft bearing diagnosis based on casing signals is challenging and the datasets of this paper deserve further fault diagnosis study.

4.3 Benchmark Study of Machine Learning

Based on the datasets collected in this paper, Convolutional Neural Networks (CNN) and Long Short-Term Memory (LSTM) models are utilized for inter-shaft bearing fault diagnosis. CNN is proven to possess a strong ability in feature extraction^[8] and LSTM excels at obtaining long-term dependencies^[17]. The structures and parameters of CNN and LSTM models are shown in Fig. 20 and Tab. 8.

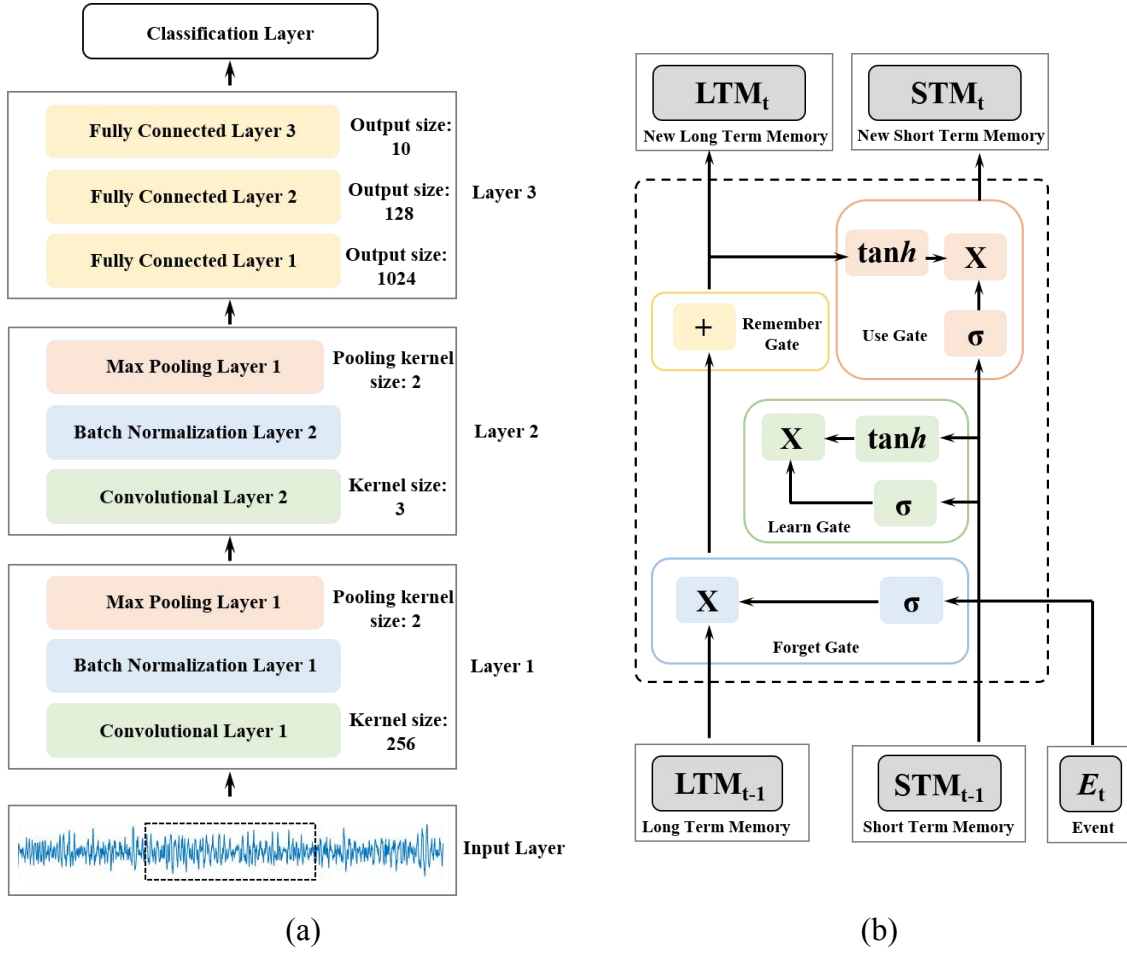


Fig. 20 Structure of (a) CNN model. (b) LSTM model.

Tab. 8 The detailed structure of CNN and LSTM models.

| Model | Structure Parameters | | |
|-------|--|---|--|
| CNN | $\text{Conv 7D}(1, 25, 256)$ [$\text{BatchNorm}(25)$ ReLU $\text{Maxpool1D}(2, 2)$] | $\text{Conv 7D}(25, 50, 3)$ [$\text{BatchNorm}(50)$ ReLU $\text{Maxpool1D}(2, 2)$] | $\text{Linear}(22350, 1024, \text{ReLU})$ $\text{Linear}(1024, 128, \text{ReLU})$ $\text{Linear}(128, 10)$ |
| LSTM | $\text{Conv 7D}(1, 128, 3)$ | $\text{LSTM}(45, 64, \tanh)$ [$\text{Dropout}(0.7)$] | $\text{Linear}(64, 128, \text{GeLU})$ $\text{Dropout}(0.7)$ $\text{Linear}(128, 10, \text{ReLU})$ |

The data from 6 channels are sequenced to generate a two-dimensional time series array for machine learning training and testing. The data were divided into training sets and test sets with 70% and 30% of the data, respectively. The CNN was trained over 40 epochs, while the LSTM was trained over 80 epochs to obtain the fault mode. The accuracy of the models was verified by testing the fault diagnosis on the test set. The boxplot of loss function values and accuracies are shown in Fig. 20 and Fig. 21.

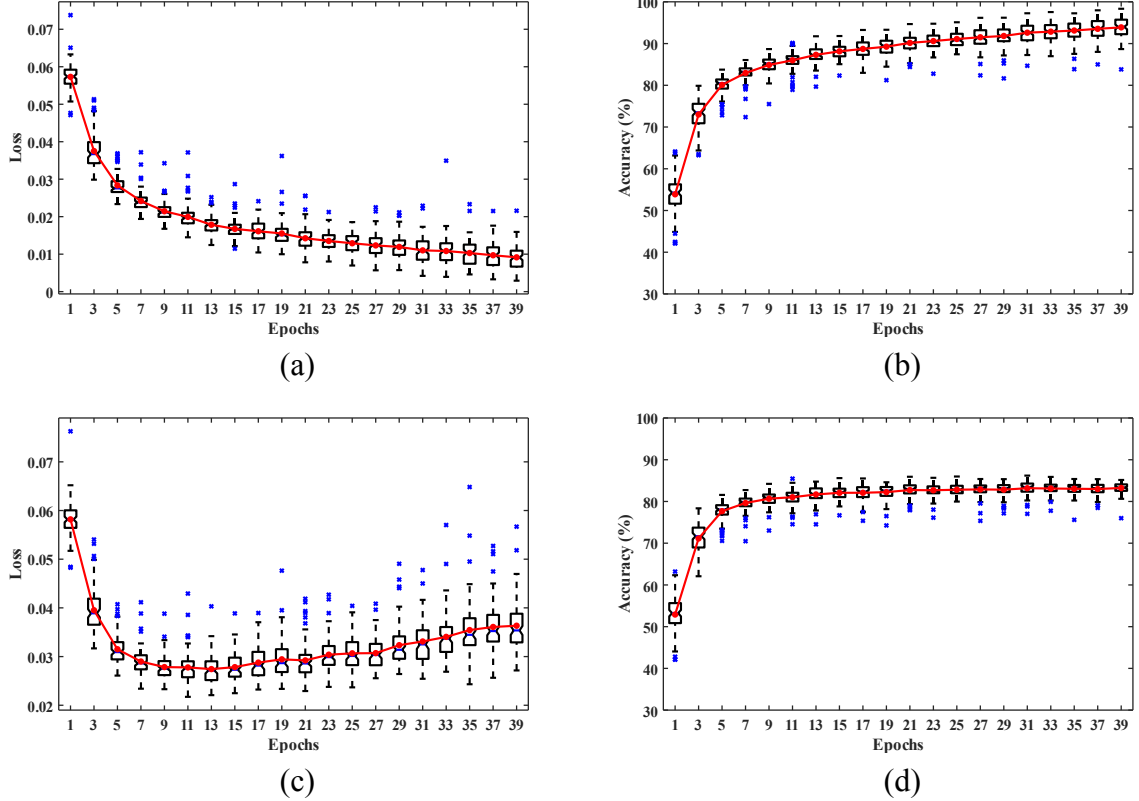
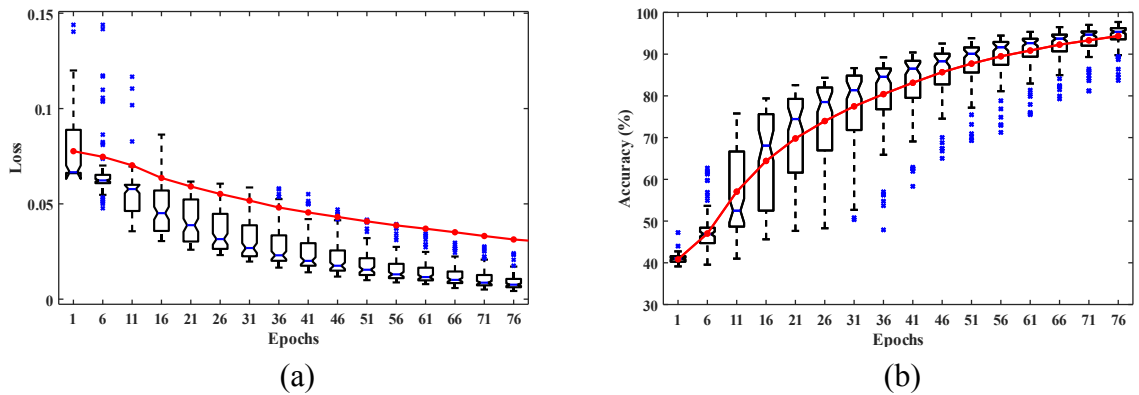


Fig. 21 The fault diagnosis results of CNN. (a) Loss function value of training set. (b) Accuracy of training set. (c) Loss function value of test set. (d) Accuracy of test set.



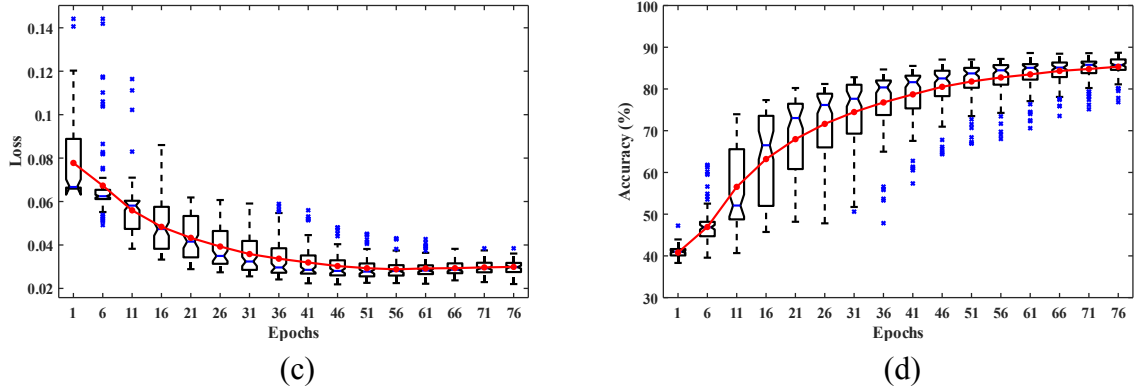


Fig. 22 The fault diagnosis results of LSTM. (a) The average loss function values of 50 epochs. (b) The average accuracy of 50 epochs.

Based on the model loss functions and accuracy diagrams of CNN depicted in Fig. 20, it is observed that the loss functions of CNN decrease gradually with an increase in epochs. The test set accuracy of CNN stabilizes at over 80% in just 10 epochs. In Fig. 20(c), the loss function of the test set increases inversely after 30 epochs, after excluding the influence factors such as overfitting, the study found that this may be caused by the structure of CNN or the influence of noise signal in the dataset. That means the fault diagnosis of this dataset deserves further in-depth research. From Fig. 21, it can be found that the loss function of the test set of LSTM decreases gradually with an increase and stabilize in 40 epochs. The test set accuracy of LSTM stabilizes at over 81% in 50 epochs, which converges more slowly but with higher accuracy than CNN. The average loss function values and accuracies of CNN and LSTM are presented in Tab. 6 and Tab. 7, respectively.

Tab. 9 The average loss function values and accuracies of CNN.

| Epochs | Average loss function values | | Average accuracy | |
|--------|------------------------------|----------|------------------|----------|
| | Training set | Test set | Training set | Test set |
| 1 | 0.0573 | 0.0582 | 53.89% | 52.91% |
| 5 | 0.0283 | 0.0315 | 80.10% | 77.67% |
| 10 | 0.0206 | 0.0277 | 85.50% | 80.93% |
| 15 | 0.0167 | 0.0278 | 88.14% | 82.07% |
| 20 | 0.0145 | 0.0293 | 89.96% | 82.71% |
| 25 | 0.0129 | 0.0307 | 91.10% | 82.82% |
| 30 | 0.0117 | 0.0330 | 92.00% | 82.84% |
| 35 | 0.0103 | 0.0354 | 93.12% | 83.04% |
| 40 | 0.0091 | 0.0376 | 94.04% | 83.13% |

Tab. 10 The average loss function values and accuracies of LSTM.

| Epochs | Average loss function values | | Average accuracy | |
|--------|------------------------------|----------|------------------|----------|
| | Training set | Test set | Training set | Test set |
| 1 | 0.0776 | 0.0778 | 40.83% | 40.81% |
| 10 | 0.0574 | 0.0580 | 55.24% | 54.78% |

| | | | | |
|----|--------|--------|--------|--------|
| 20 | 0.0420 | 0.0442 | 68.71% | 67.03% |
| 30 | 0.0322 | 0.0365 | 76.96% | 74.09% |
| 40 | 0.0250 | 0.0322 | 82.73% | 78.48% |
| 50 | 0.0188 | 0.0294 | 87.38% | 81.58% |
| 60 | 0.0142 | 0.0288 | 90.73% | 83.47% |
| 70 | 0.0108 | 0.0295 | 93.13% | 84.74% |
| 80 | 0.0085 | 0.0310 | 94.81% | 85.41% |

The traditional machine learning methods such as LSTM and CNN can achieve an accuracy of more than 80% in fault diagnosis, there is room for improvement in diagnosis accuracy. In recent years, transformers have been widely used to diagnose faults and achieve an excellent diagnostic effect. Based on the datasets, this study uses a Time Series Transformer (TST)^[28] method to diagnose inter-shaft bearing faults. The TST model structure and parameters are shown in Fig. 23 and Tab. 11. The boxplot of loss function values and accuracies are shown in Fig. 24.

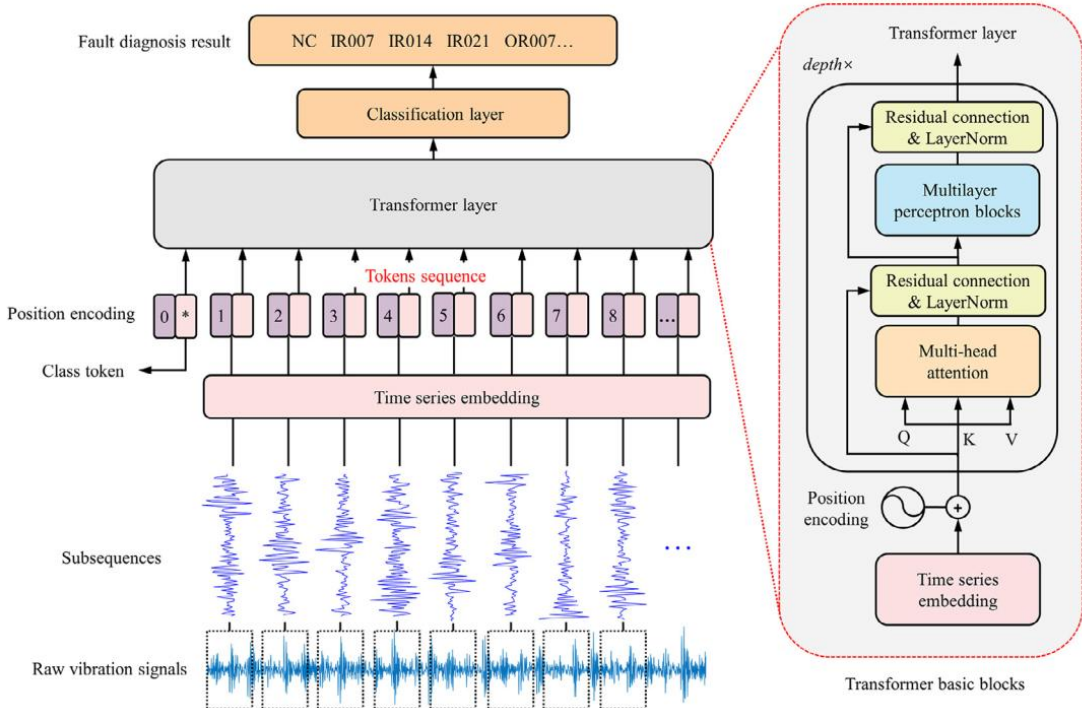


Fig. 23 Structure of TST model^[28].

Tab. 11 The detailed structure of TST model.

| Model | Structure Parameters | | | | | | | |
|-------|----------------------|---------|-------|-------------|-------|-----|---------|--------------|
| | N_s | L/N_s | dim | dim_{MLP} | d_k | h | $depth$ | Pos encoding |
| TST | 256 | 8 | 128 | 256 | 64 | 8 | 4 | 1 D |

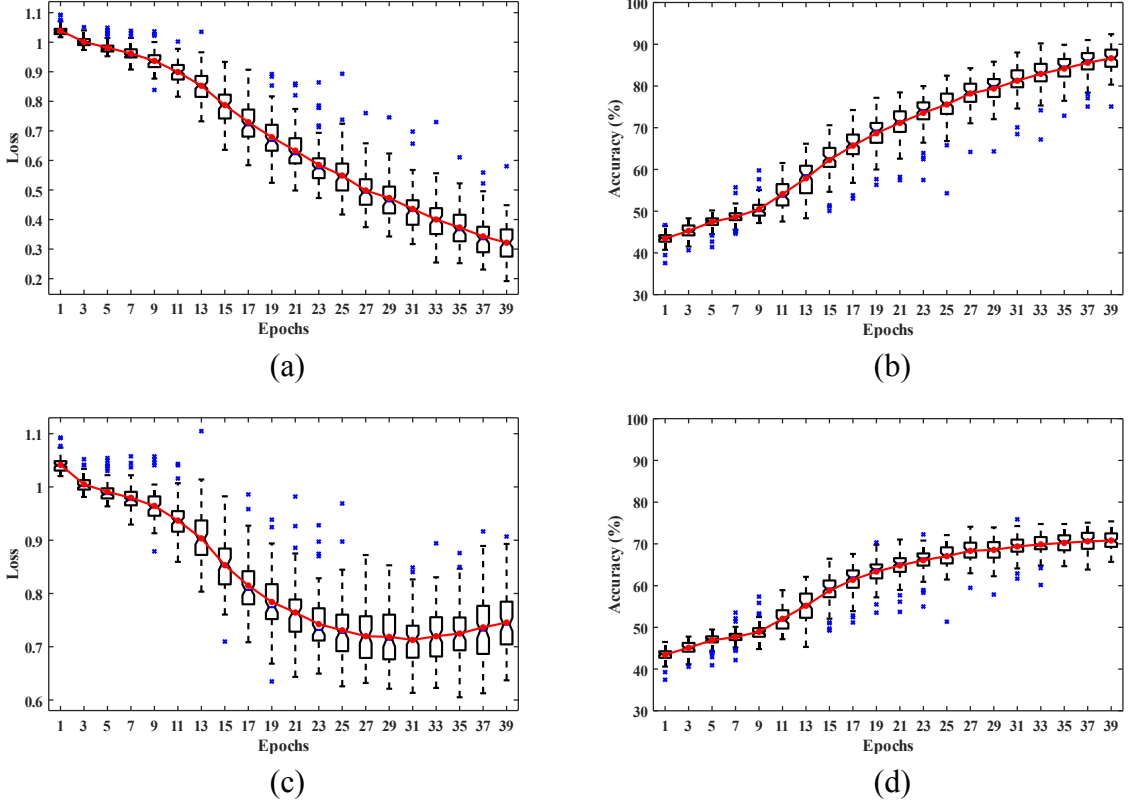


Fig. 24 The loss function values during the training of TST. (a) Box plot of 10 epochs. (b) Average values of 50 epochs.

From the diagram of the model loss function of the test set in Fig. 24(c), the loss functions of the test set and test set decrease gradually with the increase of epochs and increases inversely after 30 epochs, which may also be the effect of dataset noise or TST structure. As is shown in Fig. 24, it can be seen that the test set accuracy receives a level of more than 80% over 30 epochs, and the test set accuracy is more than 70% at 35 epochs. It can be seen that TST does not show better diagnostic efficacy compared with CNN and LSTM, which deserves further study. The average loss function values and accuracies of the training set and test set are shown in Tab. 8.

Tab. 12 The average loss function values and accuracies of TST.

| Epochs | Average loss function values | | Average accuracy | |
|--------|------------------------------|----------|------------------|----------|
| | Training set | Test set | Training set | Test set |
| 1 | 1.0388 | 1.0416 | 43.45% | 43.43% |
| 5 | 0.9815 | 0.9909 | 47.43% | 46.91% |
| 10 | 0.0918 | 0.9510 | 52.04% | 50.23% |
| 15 | 0.7871 | 0.8531 | 62.28% | 58.80% |
| 20 | 0.6546 | 0.7753 | 70.08% | 64.26% |
| 25 | 0.5486 | 0.7309 | 75.56% | 67.06% |
| 30 | 0.4536 | 0.7199 | 80.36% | 69.08% |
| 35 | 0.3731 | 0.7249 | 84.18% | 70.24% |
| 40 | 0.3086 | 0.7480 | 87.19% | 71.07% |

Comparing the diagnosis results of this dataset with those based on other datasets in

existing papers, the results are listed in Tab. 9.

Tab. 13 Comparison of the diagnosis result based on dataset of this paper and others.

| Methodology | Accuracy | | | | |
|-------------|-----------------------|--------|------------|--------|------------|
| | Dataset of this paper | CWRU | Difference | XJTU | Difference |
| CNN | 83.13% | 93.30% | (-12.23%) | 98.00% | (-17.89%) |
| LSTM | 85.41% | 92.07% | (-7.80%) | 98.65% | (-15.50%) |
| TST | 71.07% | 99.72% | (-40.31%) | 99.78% | (-40.40%) |

The results in Tab. 9 show that in the comparison of CNN, LSTM and TST, the diagnosis accuracy of the dataset in this paper is lower than that of the existing bearing datasets. Compared with the accuracy of the dataset in this paper, the accuracy difference can reach a maximum of 40.40%. All these mean that the dataset in this paper is closer to the actual engineering and more difficult to diagnose, which provides a new challenge for inspecting fault diagnosis methods.

5. Conclusions

This study built a test rig based on an aero-engine, which includes a motor drive system and a lubricant system. The vibration signals of the aero-engine under inter-shaft bearing faults were obtained by replacing the inter-shaft bearings with artificially faulty ones. The test data under different inter-shaft bearing conditions were integrated and processed to form a dataset of 2412 test data of aero-engine inter-shaft bearing faults. Based on this dataset, various methods, such as spectrum analysis, envelope spectrum analysis, CNN, LSTM, and TST, were used for fault diagnosis. The results showed that due to the difficulty of processing the signals of aero-engine housing, traditional fault diagnoses methods such as spectrum analysis and envelope spectrum analysis could not achieve effective fault diagnosis, while machine learning methods such as CNN, LSTM, and TST could achieve relatively effective fault diagnosis, but their performance is far inferior to that on existing datasets. Further study is needed to optimize the fault diagnosis method and make it more universal.

The future study can explore more effective fault diagnosis methods based on this dataset to verify the validity of the fault diagnosis methods, especially the improved methods based on the Transformer. It can also develop research in aero-engine modal parameter identification and other aspects. Furthermore, the experiment in this study is based on motor drive, and combustion drive can be tested in the future which is closer to the actual aero-engine operating state. And the bearing cage and roller faults will be a good supplement to the dataset.

Conflict of Interest

The authors declare that they have no conflict of interest.

Data availability statements

Data will be made available on request. The dataset of this paper is available at

<https://github.com/HouLeiHIT/HIT-dataset>.

Acknowledgments

The authors are very grateful for the financial supports from the National Natural Science Foundation of China (Grant No. 11972129), the Natural Science Foundation of Heilongjiang Province (Outstanding Youth Foundation, Grant No. YQ2022A008) and the Fundamental Research Funds for the Central Universities.

References

- [1] JDMD Editorial Office, N Gebraeel, Y Lei, et al. “Prognostics and remaining useful life prediction of machinery: advances, opportunities and challenges,” Journal of Dynamics, Monitoring and Diagnostics, vol.2, pp.1–12, 2023.
- [2] H Yi, L Hou, P Gao, et al. “Nonlinear resonance characteristics of a dual-rotor system with a local defect on the inner ring of the inter-shaft bearing,” Chinese Journal of Aeronautics, vol.34, pp.110-124, 2021.
- [3] S Han, Z Feng. “Deep residual joint transfer strategy for cross-condition fault diagnosis of rolling bearings,” Journal of Dynamics, Monitoring and Diagnostics, vol.2, pp.51–60, 2023.
- [4] L Hou, J Zhao, S Dun, et al. “Feature extraction of weak bearing faults based on Laplace wavelet and orthogonal matching pursuit,” Shock and Vibration, vol.2022, Art.ID.8154492, 2022.
- [5] R Yang, Z Zhang, Y Chen. “Analysis of vibration signals for a ball bearing-rotor system with raceway local defects and rotor eccentricity,” Mechanism and Machine Theory, vol.169, Art.ID.104594, 2022.
- [6] J Wang, T Li, C Sun, et al. “Improved spiking neural network for intershaft bearing fault diagnosis,” Journal of Manufacturing Systems, vol.65, pp.208-219, 2022.
- [7] M Yu, M Fang, W Chen, et al. “Compound faults feature extraction of inter-shaft bearing based on vibration signal of whole aero-engine,” Journal of Vibration and Control, vol.29, pp.51–64, 2023.
- [8] X Liu, G Chen, T Hao, et al. “A combined deep learning model for damage size estimation of rolling bearing,” International J of Engine Research, vol.24, pp.1362–1373, 2023.
- [9] X Liu, G Chen, Z Cheng, et al. “Convolution neural network based particle filtering for remaining useful life prediction of rolling bearing,” Advances in Mechanical Engineering, vol.14, pp.1–15, 2022.
- [10] W Zhang, X Ji, J Huang, et al. “Compound fault diagnosis of aero-engine rolling element bearing based on CCA blind extraction,” IEEE Access, vol.9, pp.159873-159881, 2021.
- [11] Z Hou, H Wang, S Lv, et al. “Siamese multiscale residual feature fusion network for aero-engine bearing fault diagnosis under small-sample condition,” Measurement Science and Technology, vol.34, Art.ID.035109, 2023.
- [12] X Pan, M Yu, G Meng, et al. “A study on the diagnosis of compound faults in rolling bearings based on ITD-SVD,” Journal of Vibroengineering, vol.23, pp.587-602, 2021.
- [13] H Wang, J Xu, R Yan. “Intelligent fault diagnosis for planetary gearbox using transferable deep Q network under variable conditions with small training data,” Journal of Dynamics, Monitoring and Diagnostics, vol.2, pp.30-41, 2023.
- [14] A Smith, B Randall. “Rolling element bearing diagnostics using the Case Western Reserve

University data: A benchmark study," Mechanical Systems and Signal Processing, vol.64-65, pp.100-131, 2015.

[15] B Wang, Y Lei, N Li, et al. "A hybrid prognostics approach for estimating remaining useful life of rolling element bearings," IEEE Transactions on Reliability, vol.69, pp.401-412, 2020.

[16] D Kumar, S Mehran, M Zakir, et al. "Triaxial bearing vibration dataset of induction motor under varying load conditions," Data in Brief, vol.42, Art.ID.08315, 2022.

[17] W Jung, S Kim, S Yun, et al. "Vibration, acoustic, temperature, and motor current dataset of rotating machine under varying operating conditions for fault diagnosis," Data in Brief, vol.48, Art.ID.109049, 2023.

[18] C Lessmeier, J Kimotho, D Zimmer, et al. "Condition monitoring of bearing damage in electromechanical drive systems by using motor current signals of electric motors: a benchmark data set for data-driven classification," Proceedings of the European conference of the prognostics and health management society, 2016.

[19] D Verstraete, A Ferrada, E Drogue, et al. "Deep learning enabled fault diagnosis using time-frequency image analysis of rolling element bearings," Shock and Vibration, vol.2017, pp.1-17, 2017.

[20] M Bin. "Current based condition monitoring of electromechanical systems. Model-free drive system current monitoring: faults detection and diagnosis through statistical features extraction and support vector machines classification," University of Bradford, 2013.

[21] S Porotsky. "Remaining useful life estimation for systems with non-trendability behavior," IEEE Conference on Prognostics and Health Management (PHM- 2012), 2012.

[22] S Shao, S McAleer, R Yan, et al. "Highly accurate machine fault diagnosis using deep transfer learning," IEEE Transactions on Industrial Informatics, vol.15, pp.2446-2455, 2019.

[23] P Nectoux, R Gouriveau, K Medjaher, et al. "PRONOSTIA: An experimental platform for bearings accelerated degradation tests" IEEE International Conference on Prognostics and Health Management(PHM- 2012), 2012.

[24] E Sutrisno, H Oh, A Vasan, et al. "Estimation of remaining useful life of ball bearings using data driven methodologies," IEEE Conference on Prognostics and Health Management(PHM- 2012), 2012.

[25] W Gousseau, J Antoni, F Girardin, et al. "Analysis of the rolling element bearing data set of the center for intelligent maintenance systems of the University of Cincinnati: CM2016," 2016.

[26] H Qiu, J Lee, J Lin, et al. "Wavelet filter-based weak signature detection method and its application on rolling element bearing prognostics," Journal of Sound and Vibration, vol.289, pp.1066-1090, 2006.

[27] P Cao, S Zhang, J Tang. "Preprocessing-free gear fault diagnosis using small datasets with deep convolutional neural network-based transfer learning," IEEE Access, vol.6, pp.26241-26253, 2018.

[28] Y Jin, L Hou, Y Chen. "A Time Series Transformer based method for the rotating machinery fault diagnosis," Neurocomputing, vol.494, pp. 379–395, 2022.